FAS Meets OFDM: Enabling Wideband 5G NR

Hanjiang Hong, *Member, IEEE*, Kai-Kit Wong, *Fellow, IEEE*,
Haoyang Li, *Member, IEEE*, Hao Xu, *Senior Member, IEEE*, Han Xiao, *Student Member, IEEE*,
Hyundong Shin, *Fellow, IEEE*, Kin-Fai Tong, *Fellow, IEEE*, and Yangyang Zhang

Abstract—Fluid antenna system (FAS) is an emerging technology that uses the new form of shape- and position-reconfigurable antennas to empower the physical layer for wireless communications. Prior studies on FAS were however limited to narrowband channels. Motivated by this, this paper addresses the integration of FAS in the fifth generation (5G) orthogonal frequency division multiplexing (OFDM) framework to address the challenges posed by wideband communications. We propose the framework of the wideband FAS-OFDM system that includes a novel port selection matrix. Then we derive the achievable rate expression and design the adaptive modulation and coding (AMC) scheme based on the rate. Extensive link-level simulation results demonstrate striking improvements of FAS in the wideband channels, underscoring the potential of FAS in future wireless communications.

Index Terms—5G, 6G, adaptive modulation and coding (AMC), fluid antenna system (FAS), OFDM, performance evaluation.

I. INTRODUCTION

WITH the development of fifth generation (5G) wireless communication system in full swing, the development of sixth generation (6G) mobile system is beginning to come into the limelight [1], [2]. The vision of 6G is ambitious and it aims to create a seamless reality where the digital and physical worlds merge. Achieving this vision requires new technologies to meet ambitious targets, including, for instance, a peak rate of 1 Tbps, an end-to-end latency of 1 ms, and a connection density of 10^7 devices/km^2, etc [3], [4], [5], [6].

H. Hong and K. K. Wong are with the Department of Electronic and Electrical Engineering, University College London, London, United Kingdom. K. K. Wong is also affiliated with the Department of Electronic Engineering, Kyung Hee University, Yongin-si, Gyeonggi-do 17104, Republic of Korea (e-mail: hanjiang.hong, kai-kit.wong @ucl.ac.uk).

H. Li is with the Cooperative Medianet Innovation Center (CMIC), Shanghai Jiao Tong University, Shanghai 200240, China (e-mail: li-haoyang@sjtu.edu.cn).

H. Xu is with the National Mobile Communications Research Laboratory, Southeast University, Nanjing 210096, China (e-mail: hao.xu@seu.edu.cn).

H. Xiao is School of Information and Communications Engineer- ing, Xi'an Jiao Tong University, China (e-mail: hanxiaonuli@stu.xjtu.edu.cn).

H. Shin is with the Department of Electronics and Information Convergence Engineering, Kyung Hee University, 1732 Deogyeong-daero, Giheung-gu, Yongin-si, Gyeonggi-do 17104, Republic of Korea (e-mail: hshin@khu.ac.kr).

K. F. Tong is with the School of Science and Technology, Hong Kong Metropolitan University, Hong Kong SAR, China (e-mail: ktong@hkmu.edu.hk).

Y. Zhang is with Kuang-Chi Science Limited, Hong Kong SAR, China (e-mail: yangyang.zhang@kuang-chi.com).

Corresponding author: Kai-Kit Wong and Hyundong Shin.

One of the promising candidates emerging in this effort is fluid antenna system (FAS) [7], [8], [9], [10], which leverages the spatial diversity fully in a given spatial region to increase the degree-of-freedom (DoF) in the physical layer for a variety of benefits [11]. Concisely, FAS is a broad concept that utilizes the new form of shape- and position-reconfigurable antennas for wireless communications. In [12], the definition of fluid antenna was explained using electromagnetic theory. It should be noted that recent terminologies such as movable antennas [13], flexible-position antenna systems [14] and pinching antennas [15] are well within the definition of FAS.

FAS was first introduced by Wong *et al.* in [16], [17] when the benefits of a position-flexible antenna at a receiver over wireless channels were studied and highlighted. These seminal works were greatly motivated by reconfigurable antennas such as liquid-metal antennas [18], [19], [20], movable arrays [21], metamaterial-based antennas [22], [23], [24], radio-frequency (RF) pixel-based antennas [25] and etc. Clearly, FAS is not restricted to any specific implementation techniques.[1]

Since the early works in [16], [17], there have been numerous attempts in advancing the research of FAS. For instance, performance analysis for FAS has been investigated by using an eigenvalue-based channel model in [26]. The diversity order of a FAS receiver channel was examined in [27]. Additionally, [28] developed a block-correlation model to greatly simplify the performance analysis of FAS. Subsequent analyses further extended the analysis to Nakagami fading channels [29], [30], and α-μ fading channels [31]. In [32], the authors considered a multiple-input multiple-output (MIMO) channel with FAS at both ends and derived the diversity and multiplexing tradeoff. Channel estimation is a key aspect for FAS. Recent inquiries into channel estimation for FAS channels have acknowledged the significance of spatial correlation [33], [34], [35], [36] and spatial oversampling [37]. The interest of FAS has also grown into its application for secrecy communication [38], [39], [40], its synergy with reconfigurable intelligent surface (RIS) [41], [42], [43], [44], and its advantages for integrated sensing and communication (ISAC) [45], [46], [47].

Furthermore, FAS demonstrates great potential for multiuser communications. The idea is that by exploiting antenna position reconfigurability, FAS can access the received signal in which the interference suffers from a deep fade occurred due to the multipath phenomenon. This has led to the concept of fluid antenna multiple access (FAMA) first proposed in [48]. Thus far, there have been several variants of FAMA including slow [49], [50], [51] and coded [52], [53]. It is also possible to combine slow FAMA with analogue signal mixing to improve

---

[1]The word 'fluid' in FAS is meant to highlight the flexible nature of the antenna but does not imply the use of fluidic materials for antenna.

This article has been accepted for publication in IEEE Transactions on Communications. This is the author's version which has not been fully edited and content may change prior to final publication. Citation information: DOI 10.1109/TCOMM.2025.3591751

2

the interference immunity [54], [55]. What makes FAMA an attractive approach is that both interference cancellation at the receiver and precoding at the transmitter are not needed.

Despite the progress so far, the above-mentioned researches were focused on narrowband channels. However, in practical environments, delay spread can be significant, necessitating the use of orthogonal frequency-division multiplexing (OFDM). Technically speaking, there are ongoing concerns if FAS could still perform well under OFDM settings, due to the potential variability in characteristics among the subcarriers. Recently, [56] has combined FAS and OFDM at the transmitter for index modulation while [57] also attempted to examine wideband FAS transmission with an emphasis on optimizing the antenna positions. However, so far not much is understood regarding the integration of FAS into the 5G New Radio (NR) settings, along with the coding and modulation procedures.

Motivated by this, this paper aims to integrate FAS into the NR OFDM framework. In particular, we present a framework for FAS-OFDM that addresses wideband channels and introduce a novel port selection metric specifically designed for this system. Furthermore, an adaptive modulation and coding (AMC) mechanism tailored to this system is proposed. Importantly, the proposed system is contextualized within the 5G NR environment, where we conduct link-level simulations to assess the block error rate (BLER) over the 3rd Generation Partnership Project (3GPP) wideband channels.

Our main contributions are summarized as follows:

- First, we develop a framework of wideband FAS-OFDM systems, complemented by a novel port selection metric specifically designed for this system. This metric efficiently maps the polymorphic channels in the frequency domain to a distinct channel indicator, thereby enabling FAS to judiciously adjust the antenna port.

- Additionally, we derive the average symbol error probability (ASEP) and the bit-interleaved coded modulation (BICM) capacity for the narrowband FAS system. Then based on the proposed wideband port selection metric, we extend the BICM capacity analysis to the FAS-OFDM system, which quantifies the achievable rate of the system. Furthermore, we investigate the AMC mechanism relevant to the FAS-OFDM system, utilizing the derived BICM capacity to calculate the average effective signal-to-noise ratio (SNR) for the system.

- The proposed FAS-OFDM framework, encompassing the port selection metric and AMC mechanism, is integrated into 5G NR. 5G NR numerologies [58], channel coding [59], and OFDM modulation [60] are all adopted in alignment with the latest standards. Link-level simulations are conducted based on the tapped delay line (TDL) channel model from 3GPP [61] in order to provide an accurate performance evaluation for the FAS-OFDM system.

The remainder of the paper is organized as follows. Section II introduces the system model of the wideband FAS-OFDM system. The port selection, BICM capacity, and AMC mechanism of the FAS-OFDM system are illustrated in Section III. Section IV specifies the implementation details of 5G NR, and presents the link-level simulation results of the wideband FAS-OFDM system. Conclusions are drawn in Section V.

Notations: Scalars are represented by lowercase letters while vectors and matrices are denoted by lowercase and uppercase boldface letters, respectively. Transpose and hermitian operations are denoted by superscript T and $\dagger$, respectively. For a complex scalar x, $|x|$ and $x^\dagger$ denote its modulus and conjugate, respectively. For a set $\boldsymbol{\chi}$, $|\boldsymbol{\chi}|$ represents its cardinality.

II. SYSTEM MODEL

In this paper, we consider a point-to-point FAS-aided communication system as depicted in Fig. 1. The transmitter is equipped with a single conventional fixed position antenna (FPA) to ensure backward compatibility, while the receiver utilizes a FAS with one activated port to enhance performance.

At the transmitter side, the bit stream $\boldsymbol{b} = \{b_0, \ldots, b_{N_a-1}\}$ is encoded to a bit sequence $\boldsymbol{c} = \{c_0, \ldots, c_{N_b-1}\}$, with a code rate of CR $= N_a/N_b$. Subsequently, the encoded bit sequence $\boldsymbol{c}$ is scrambled to randomize the date pattern. The resultant scrambled bit sequence $\boldsymbol{d} = \{d_0, \ldots, d_{N_b-1}\}$ is then mapped by a constellation $\boldsymbol{\chi}$ into a symbol sequence $\boldsymbol{x} = \{x[0], \ldots, x[N_s - 1]\}$, where $N_s = N_b/Q_m$ represents the length of constellation symbols, and $Q_m = \log_2|\boldsymbol{\chi}|$. Here, normalized constellations are assumed. That is, the average symbol energy is one, or

$$E_x = \frac{1}{|\boldsymbol{\chi}|} \sum_{x \in \boldsymbol{\chi}} |x|^2 = 1. \tag{1}$$

The system can support various code rates and constellations (e.g., quadrature phase shift keying (QPSK), 16 quadrature amplitude modulation (QAM), and 64-QAM, etc.). The symbol sequence $\boldsymbol{x}$ is subsequently used to generate the waveform for transmission. The transmitting waveform generation module may comprise resource mapping and OFDM modulation.

The receiver has a $K = (K_1 \times K_2)$-port two-dimensional FAS (2D-FAS) with a physical size of $W = W_1\lambda \times W_2\lambda$, where λ denotes the carrier wavelength. Note that we use λ for simplicity in our discussion, but the physical size of FAS does not have a direct relationship with λ. Across the 2D space, K_i ports are uniformly positioned along a linear space of length $W_i\lambda$ for $i \in \{1, 2\}$. For the sake of simplicity, we define the mapping of the antenna port $(k_1, k_2) \to k : k = k_1 \times K_2 + k_2$, where $k_1 \in \{0, \ldots, K_1 - 1\}$, $k_2 \in \{0, \ldots, K_2 - 1\}$, and $k \in \{0, \ldots, K - 1\}$. Utilizing FAS, the received antenna can switch to the port, k^*, exhibiting the highest SNR to effectively receive the signal sequence $\boldsymbol{r}_{k^*}$. This sequence is then reversed to form a symbol sequence $\boldsymbol{y} = \{y[0], \ldots, y[N_s - 1]\}$, which is then demapped to the log-likelihood ratio (LLR) sequence $\boldsymbol{l} = \{L_0, \ldots, L_{N_b-1}\}$. The soft information $\boldsymbol{l}$ is subsequently passed to the de-scrambler and decoder for the recovery of the data bits $\hat{\boldsymbol{b}} = \{\hat{b}_0, \ldots, \hat{b}_{N_a-1}\}$.

A. Narrowband FAS Channel Model

In the context of narrowband FAS, the n-th received symbol at the k-th port can be expressed as

$$y_k[n] = h_k x[n] + \eta_k[n], \tag{2}$$

where h_k denotes the channel coefficient at the k-th port, and $\eta_k[n]$ is the zero-mean complex Gaussian noise with a variance
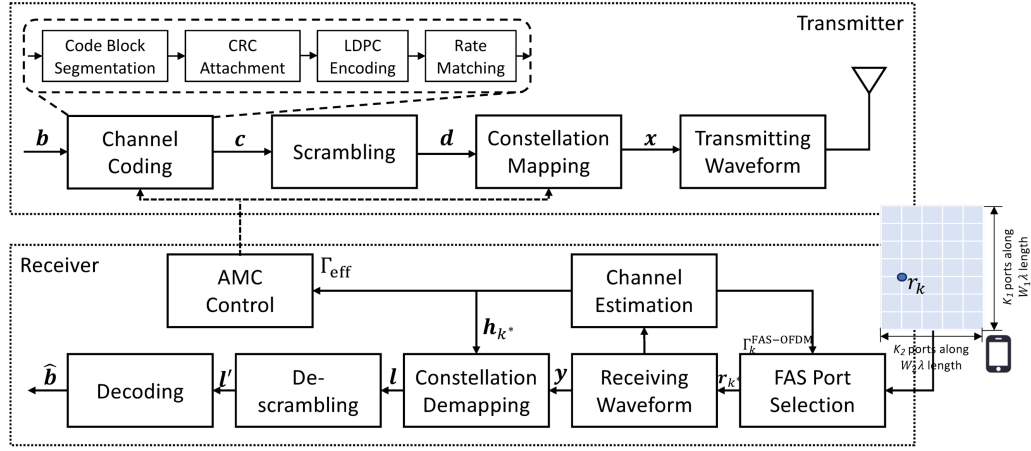
Fig. 1. System model of the point-to-point FAS communication system.

of σ_η^2. The received symbol from all the antenna ports can be consolidated into vector form as

$$\boldsymbol{y}[n] = \boldsymbol{h}x[n] + \boldsymbol{\eta}[n], \tag{3}$$

where $\boldsymbol{y}[n] = [y_0[n], \ldots, y_{K-1}[n]]^T$, $\boldsymbol{h} = [h_0, \ldots, h_{K-1}]^T$, and $\boldsymbol{\eta}[n] = [\eta_0[n], \ldots, \eta_{K-1}[n]]^T$. We assume that the channels suffer from block fading, which implies that $\boldsymbol{h}$ fluctuates yet remains constant during the transmission of block $\boldsymbol{x}$. In addition, the channels $\{h_k\}_{\forall k}$ exhibit correlation. Utilizing the eigenvalue-based model in [26] and assuming a rich scattering environment, h_k can be expressed as

$$h_k = \sigma_h \sum_{l=0}^{K-1} \sqrt{\lambda_l} \mu_{k,l} g_l, \tag{4}$$

where $g_l \sim \mathcal{CN}(0,1)$, λ_l and $\mu_{k,l}$ are derived from the singular value decomposition (SVD) of the channel covariance matrix $\boldsymbol{\Sigma}$, with $\mathbb{E}[\boldsymbol{hh}^\dagger] = \sigma_h^2 \boldsymbol{\Sigma}$, and we have

$$[\boldsymbol{\Sigma}]_{k,l} = J_0 \left(2\pi \sqrt{ \left(\frac{k_1 - l_1}{N_1 - 1} W_1 \right)^2 + \left(\frac{k_2 - l_2}{N_2 - 1} W_2 \right)^2 } \right), \tag{5}$$

where $(l_1, l_2) \to l$, and $J_0(\cdot)$ is the zero-order Bessel function of the first order. SVD is carried out as $\boldsymbol{\Sigma} = \boldsymbol{U\Lambda U}^\dagger$, where $\boldsymbol{\Lambda} = \mathrm{diag}(\lambda_0, \ldots, \lambda_{K-1})$ and $[\boldsymbol{U}]_{k,l} = \mu_{k,l}$.

The received SNR at the k-th port is given by

$$\Gamma_k = |h_k|^2 \frac{E_x}{\sigma_\eta^2} = |h_k|^2 \Theta, \tag{6}$$

where $\Theta \triangleq \frac{E_x}{\sigma_\eta^2}$. Assuming perfect knowledge of the channel coefficients $\{|h_k|\}_{\forall k}$, the FAS port selection process can be optimized to switch the antenna to the port k^* that provides the maximum received SNR, i.e.,

$$k^* = \arg \max_k |h_k|. \tag{7}$$

B. Wideband FAS-OFDM Channel Model

In this paper, however, the focus is primarily on the wideband FAS-OFDM system, wherein the symbol sequence $\boldsymbol{x}$ is mapped to a symbol grid comprising N OFDM symbols and F subcarriers. The cyclic prefix (CP) eliminates inter-symbol interference (ISI) and accommodates simple frequency-domain processing. At the n-th OFDM symbol, the wideband FAS channel can be modelled in the frequency domain as

$$
\begin{bmatrix} \boldsymbol{y}[0,n] \\ \boldsymbol{y}[1,n] \\ \vdots \\ \boldsymbol{y}[F-1,n] \end{bmatrix} = \begin{bmatrix} \boldsymbol{h}[0,n] & \boldsymbol{0} & \cdots & \boldsymbol{0} \\ \boldsymbol{0} & \boldsymbol{h}[1,n] & \cdots & \boldsymbol{0} \\ \vdots & \vdots & \ddots & \vdots \\ \boldsymbol{0} & \boldsymbol{0} & \cdots & \boldsymbol{h}[F-1,n] \end{bmatrix}
$$
$$
\times \begin{bmatrix} x[0,n] \\ x[1,n] \\ \vdots \\ x[F-1,n] \end{bmatrix} + \begin{bmatrix} \boldsymbol{\eta}[0,n] \\ \boldsymbol{\eta}[1,n] \\ \vdots \\ \boldsymbol{\eta}[F-1,n] \end{bmatrix}, \tag{8}
$$

where $\boldsymbol{y}[f,n] = [y_0[f,n], \ldots, y_{K-1}[f,n]]^T$ denotes the received symbol vector, $\boldsymbol{h}[f,n] = [h_0[f,n], \ldots, h_{K-1}[f,n]]^T$ denotes the channel vector, $x[f,n]$ denotes the transmitted symbol, and $\boldsymbol{\eta}[f,n] = [\eta_0[f,n], \ldots, \eta_{K-1}[f,n]]^T$ denotes the complex noise vector at the f-th subcarrier and n-th OFDM symbol, respectively, for $0 \leq n < N$ and $0 \leq f < F$. The channel is subject to frequency-selective fading when $\boldsymbol{h}[f,n]$ varies over f, and time-selective fading when $\boldsymbol{h}[f,n]$ varies over n. The channels $\{h_k[n,f]\}_{\forall k}$ are also correlated amongst the antenna ports, leading to the covariance matrix as $\mathbb{E}\{\boldsymbol{h}[f,n]\boldsymbol{h}^\dagger[f,n]\} = \sigma_h^2 \boldsymbol{\Sigma}$, where the elements in $\boldsymbol{\Sigma}$ are specified in (5). Notably, when $\boldsymbol{h}[f,n] = \boldsymbol{h}, \forall f \in [0,F), n \in [0,N)$, i.e., the channel is subject to flat fading, the wideband channel model in (8) reduces to that expressed in (3).

In the wideband FAS-OFDM system, as shown in Fig. 1, the receiving waveform module transfers the received signal from the time domain to the frequency domain. The FAS port selection is proceeded in the time domain, while the channel estimation, demapping, and decoding processes are conducted in the frequency domain. It is impractical for FAS to switch the antenna ports instantaneously in response to frequency-selective fading, as the system cannot select different physical ports in the time domain for distinct frequency-domain subcarriers. Therefore, the development of a novel port selection metric is imperative to encure the selection of

an appropriate port that impacts the performance of multiple subcarriers within the wideband FAS-OFDM system.

III. PORT SELECTION FOR FAS-OFDM

In this section, we propose a novel port selection metric for the wideband FAS-OFDM system. The ASEP and BICM capacity of the FAS system are derived accordingly. The analysis of BICM capacity is then extended to the FAS-OFDM system utilizing the proposed metric, and the AMC mechanism is introduced based on the derived BICM capacity.

A. Port Selection

Here, we discuss the port selection process, as modeled by (8). Given the assumption of a perfect knowledge of the three-dimensional $K \times N \times F$ channel grid $\boldsymbol{H} = \{\boldsymbol{h}[f,n]\}_{\forall n,f}$, the port selection of FAS-OFDM system requires the formulation of a metric, $\Gamma_k^{\text{FAS-OFDM}}$, to evaluate the antenna ports and then identify the strongest one (i.e., port k^*) by

$$k^* = \arg\max_k \Gamma_k^{\text{FAS-OFDM}}. \tag{9}$$

This performance metric, $\Gamma_k^{\text{FAS-OFDM}}$, requires the ability to effectively capture the polymorphic channels $\{h_k[f,n]\}_{\forall f,n}$ and represent them in an alternative single-channel format. Specifically, it can be expressed as

$$\Gamma_k^{\text{FAS-OFDM}} = \beta \Psi^{-1}\left(\frac{1}{NF}\sum_{n=0}^{N-1}\sum_{f=0}^{F-1}\Psi\left(\frac{\Gamma_k[f,n]}{\beta}\right)\right), \tag{10}$$

where $\Psi(\cdot)$ represnets a compression function for the SNR mapping, $\Psi^{-1}(\cdot)$ denotes the inverse function of $\Psi(\cdot)$, β acts as a scale factor to adjust the compression function when there is a mismatch, and $\Gamma_k[f,n]$ is the received SNR of n-th OFDM symbol and the f-th subcarrier, given by

$$\Gamma_k[f,n] = |h_k[f,n]|^2 \Theta. \tag{11}$$

A crucial component of the performance metric (10) is the design of compression function $\Psi(\cdot)$. Various SNR mapping metrics may be considered, including exponential SNR mapping or mutual information SNR mapping. Mutual information SNR mapping typically provides the best accuracy, although it comes at a higher computational cost. For this reason, a straightforward approach is to set $\beta = 1$, and $\Psi(x) = x$, resulting in the average SNR mapping given by

$$\Gamma_k^{\text{ave}} = \frac{1}{NF}\sum_{n=0}^{N-1}\sum_{f=0}^{F-1}\Gamma_k[f,n]$$
$$= \frac{\Theta}{NF}\sum_{n=0}^{N-1}\sum_{f=0}^{F-1}|h_k[h,n]|^2. \tag{12}$$

By using this average SNR mapping metric, the port selection in (9) can be reformulated as

$$k_{\text{ave}}^* = \arg\max_k \frac{\Theta}{NF}\sum_{n=0}^{N-1}\sum_{f=0}^{F-1}|h_k[h,n]|^2. \tag{13}$$

The average SNR in (12) corresponds to the carrier-to-noise ratio (CNR). In this case, the port selection can be performed within the frequency domain based on the CNR measurements, leading to a reduction in receiver complexity.

Note that when the channel is subject to flat fading, i.e., $\boldsymbol{h}[f,n] = \boldsymbol{h}, \forall f,n$, the selection mapping metric in (13) degenerates to the FAS port selection metric in (7).

In this paper, we assume perfect channel state information (CSI) knowledge for all FAS ports at the receiver. When CSI is unknown in the practical system, several training subframes are required to estimate $\{h_k\}_{\forall k}$, while the RF chain switches among ports on a subframe basis. But the transmission is not disrupted during the training stage. These training subframes can transmit signals at a rate that is the same as or slightly higher than that of the FPA-based system [53]. Advanced channel estimation techniques, such as [33], [34], [35], [36], [37], contribute to improving the accuracy and reducing the overhead of channel estimation for FAS.

B. ASEP and BICM Capacity for Narrowband System

Here, we first present our analysis of ASEP and BICM capacity in narrowband FAS channels, i.e., the model in (4).

With port selection in (7), the received symbol y_{k^*}, with time index omitted, can be expressed as

$$y_{k^*} = h_{k^*}x + \eta_{k^*}. \tag{14}$$

Thus, the equalized symbol is given by

$$\tilde{x} = \frac{h_{k^*}^\dagger}{|h_{k^*}|^2}y_{k^*} = x + \frac{h_{k^*}^\dagger}{|h_{k^*}|^2}\eta_{k^*}. \tag{15}$$

Here, the noise variance is calculated as

$$\tilde{\sigma}^2 = \sigma_\eta^2/h_{\text{FAS}}^2, \tag{16}$$

where $h_{\text{FAS}} = |h_{k^*}| = \max\{|h_0|, \ldots, |h_{K-1}|\}$ for simplicity.

In the uncoded system, the received symbol is detected by the maximum likelihood detector as $\hat{x} = \arg\min_{x \in \boldsymbol{\chi}}|\tilde{x} - x|^2$. Based on the detector, the h_{FAS}-dependent instantaneous symbol error probability (SEP) for a QAM constellation $\boldsymbol{\chi}$ is given as [62]

$$P_E(h_{\text{FAS}}) = \frac{4(\sqrt{|\boldsymbol{\chi}|}-1)}{\sqrt{|\boldsymbol{\chi}|}}Q\left(\sqrt{\frac{3E_x h_{\text{FAS}}^2}{(|\boldsymbol{\chi}|-1)\sigma_\eta^2}}\right)$$
$$- \frac{4(\sqrt{|\boldsymbol{\chi}|}-1)^2}{|\boldsymbol{\chi}|}Q^2\left(\sqrt{\frac{3E_x h_{\text{FAS}}^2}{(|\boldsymbol{\chi}|-1)\sigma_\eta^2}}\right), \tag{17}$$

where $Q(\cdot)$ is the Gaussian Q-function. The statistical expectation of instantaneous SEP with respect to h_{FAS} yields the expression for ASEP, as

$$\bar{P}_E = \mathbb{E}\{P_E(h_{\text{FAS}})\} = \int_0^\infty P_E(r)p_{h_{\text{FAS}}}(r)dr, \tag{18}$$

where $p_{h_{\text{FAS}}}(r)$ is the probability density function (PDF) of h_{FAS}. The PDF analysis based on the channel model (4) is tricky since the channel of each port includes N intertwined random variables. But it can be approximated by using the *First Stage approximation* in [26, Definition 1], as

$$h_k \approx \tilde{h}_k = \sigma_h\sum_{l=0}^{K_\epsilon-1}\sqrt{\lambda_l}\mu_{k,l}g_l + \sigma_h\sqrt{1-\sum_{l=0}^{K_\epsilon-1}\lambda_l\mu_{k,l}^2}\tilde{g}_k, \tag{19}$$

This article has been accepted for publication in IEEE Transactions on Communications. This is the author's version which has not been fully edited and content may change prior to final publication. Citation information: DOI 10.1109/TCOMM.2025.3591751

5

where $\tilde{g}_k \sim \mathcal{CN}(0,1)$, and K_ϵ is the number of eigenvalues $\{\lambda_0, \ldots, \lambda_{K-1}\}$ exceeding a threshold $\epsilon > 0$. Then the approximated cumulative distribution function (CDF) of h_{FAS} is given by [26, Theorem 4]. Thus, we can derive the PDF as (21) at the top of next page, where $Q_1(\cdot, \cdot)$ denotes the Marcum Q-function of order 1, $I_0(\cdot)$ is the modified Bessel function of the first kind, a_k and b_k are given by

$$\begin{cases} a_k = \sigma_h^2 \left| \sum_{l=0}^{K_\epsilon-1} \sqrt{\lambda_l} \mu_{k,k} g_k \right|^2, \\ b_k = \frac{\sigma_h^2}{2} \left(1 - \sum_{l=0}^{K_\epsilon-1} \lambda_l \mu_{k,l}^2 \right). \end{cases} \quad (20)$$

By substituting (21) into (18), we obtain the approximated ASEP in (22) at the top of next page.

In the coded system, a closed-form expression for the error probability cannot be obtained. Instead, the performance can be evaluated via the achievable rate indicator, such as the average mutual information (AMI, also known as BICM capacity) [63]. The BICM capacity conditioned on h_{FAS} is given by (24) at the top of next page, where the conditional PDF $p(\tilde{x}|x, h_{\text{FAS}})$ is given by

$$p(\tilde{x}|x, h_{\text{FAS}}) = \frac{1}{\pi \tilde{\sigma}^2} \exp\left(-\frac{|\tilde{x} - x|^2}{\tilde{\sigma}^2} \right), \quad (23)$$

with the noise variance $\tilde{\sigma}^2$ given in (16). Considering the PDF of h_{FAS} in (21), the BICM capacity of the system can be derived as (25) (see top of next page).

C. Achievable Rate for Wideband System

In this subsection, we extend the BICM capacity analysis to wideband channels, i.e., the channel model in (8).

By utilizing the port selection in (9), the channel grid with the selected k^* port is denoted as $\boldsymbol{H} = [h_{k^*}[f, n]]_{F \times N}$. The received symbol $y_{k^*}[f, n]$ for the f-th subcarrier and the n-th OFDM symbol can be expressed as

$$y_{k^*}[f, n] = h_{k^*}[f, n] x[f, n] + \eta_{k^*}[f, n]. \quad (26)$$

The minimum mean-square-error (MMSE) equalized symbol $\tilde{x}[f, n]$ is calculated as

$$\begin{aligned} \tilde{x}[f, n] &= \beta w[f, n] y_{k^*}[f, n] \\ &= \beta w[f, n] h_{k^*}[f, n] x[f, n] + \beta w[f, n] \eta_{k^*}[f, n], \quad (27) \end{aligned}$$

where $w[f, n]$ represnets the MMSE factor derived from the channel coefficients, expressed as

$$w[f, n] = \frac{h_{k^*}^\dagger[f, n]}{h_{k^*}^\dagger[f, n] h_{k^*}[f, n] + \sigma_\eta^2}, \quad (28)$$

and β denotes the normalized factor calculated as

$$\begin{aligned} \beta &= \sqrt{1/\mathbb{E}_{f,n} \left\{ |w[f, n] h_{k^*}[f, n]|^2 \right\}} \\ &= \sqrt{\frac{NF}{\sum_{n=0}^{N-1} \sum_{f=0}^{F-1} |w[f, n] h_{k^*}[f, n]|^2}}. \quad (29) \end{aligned}$$

Within the equalized expression (27), the term $\beta w h_{k^*} x$ is the desired signal component, whereas $\beta w \eta_{k^*}$ corresponds to the noise component. The noise power can be found as

$$\begin{aligned} \tilde{\sigma}^2 &= \mathbb{E}_{f,n} \left\{ |\beta w[f, n] \eta_{k^*}[f, n]|^2 \right\} \\ &= \frac{\beta^2 \sigma_\eta^2}{NF} \sum_{n=0}^{N-1} \sum_{f=0}^{F-1} |w[f, n]|^2. \quad (30) \end{aligned}$$

Thus, the average received SNR $\overline{\Gamma}$ can be formulated as

$$\begin{aligned} \overline{\Gamma} &= \frac{\mathbb{E}_{f,n} \left\{ |\beta w[f, n] h_{k^*}[f, n] x[f, n]|^2 \right\}}{\mathbb{E}_{f,n} \left\{ |\beta w[f, n] \eta_{k^*}[f, n]|^2 \right\}} \\ &= \frac{NF\Theta}{\beta^2 \sum_{n=0}^{N-1} \sum_{f=0}^{F-1} |w[f, n]|^2}. \quad (31) \end{aligned}$$

Utilizing this average received SNR $\overline{\Gamma}$, the channel capacity of the FAS-OFDM system can be derived as $C = \log_2(1+\overline{\Gamma})$.

More specifically, the BICM capacity $I_{\boldsymbol{\chi}}(\boldsymbol{H})$ for a given constellation $\boldsymbol{\chi}$ of this channel can be articulated as (32) (see top of next page), where the PDF $p(\tilde{x}|x, h_{k^*})$ is given by (23) with the noise variance given by (30). The BICM capacity of the FAS-OFDM system can be computed as the expectation over the channel grid $\boldsymbol{H}$, i.e.,

$$I_{\text{FAS-OFDM},\boldsymbol{\chi}} = \mathbb{E}_{\boldsymbol{H}} \left[I_{\boldsymbol{\chi}}(\boldsymbol{H}) \right]. \quad (33)$$

If the channel is in flat fading, i.e., $h_{k^*}[f, n] = h_{k^*}, \forall f, n$, the BICM capacity deteriorates to integral form as in (25).

D. AMC Mechanism

The objective of AMC is to allow the FAS-OFDM system to dynamically adjust its constellation and channel code rate based on real-time channel conditions, hence enhancing both reliability and efficiency in communication.

In an ideal system in which AMC can be seamlessly controlled, modulation and code rates are derived by maximizing the BICM capacity, as articulated in (32). The BICM capacity corresponding to multiple modulation constellations $\{\boldsymbol{\chi}_i\}$ is calculated to identify the optimal constellation $\boldsymbol{\chi}_{\text{opt}}$, which offers the highest capacity. Hence, the corresponding code rate is then determined as $\text{CR} = I_{\boldsymbol{\chi}_{\text{opt}}}(\boldsymbol{H}) / \log_2 |\boldsymbol{\chi}_{\text{opt}}|$.

Nevertheless, achieving a truly seamless AMC in practice is often challenging. In the pragmatic system, the AMC control process generates feedback in the form of the Channel Quality Index (CQI), which is transmitted back to the transmitter side. The precision of AMC relies heavily on the accuracy of the CQI's bit representation. The implementation process of CQI feedback follows several steps:

- **Creation of a look-up table (LUT)**: This table connects SNR to CQI based on computer simulations conducted in the additive white Gaussian noise (AWGN) channel;
- **Effective SNR calculation**: The effective SNR, Γ_{eff}, for the FAS-OFDM system is calculated, and this effective SNR is mapped to the approaching CQI value using the pre-defined LUT;
- **CQI transmission**: The computed CQI is then sent to the transmitter side, which selects the proper modulation constellation and code rate based on the received CQI.

$$p_{h_{\mathrm{FAS}}}(r) \approx \frac{1}{\pi^{K_\epsilon}} \iint_{\mathbb{C}} \cdots \iint_{\mathbb{C}} \exp\left(-\sum_{l=0}^{K_\epsilon-1} |g_l|^2\right)$$
$$\times \sum_{k=0}^{K-1} \frac{r}{b_k} \exp\left(-\frac{r^2+a_k}{2b_k}\right) I_0\left(\frac{\sqrt{a_k}}{b_k}r\right) \prod_{\substack{\tilde{k}=0 \\ \tilde{k}\neq k}}^{K-1} \left[1 - Q_1\left(\sqrt{\frac{a_{\tilde{k}}}{b_{\tilde{k}}}}, \frac{r}{\sqrt{b_{\tilde{k}}}}\right)\right] dg_0 \cdots dg_{K_\epsilon-1} \tag{21}$$

$$\bar{P}_E \approx \frac{1}{\pi^{K_\epsilon}} \int_0^\infty \iint_{\mathbb{C}} \cdots \iint_{\mathbb{C}} \left[\frac{4(\sqrt{|\boldsymbol{\chi}|}-1)}{\sqrt{|\boldsymbol{\chi}|}} Q\left(\sqrt{\frac{3E_x r^2}{(|\boldsymbol{\chi}|-1)\sigma_\eta^2}}\right) - \frac{4(\sqrt{|\boldsymbol{\chi}|}-1)^2}{|\boldsymbol{\chi}|} Q^2\left(\sqrt{\frac{3E_x r^2}{(|\boldsymbol{\chi}|-1)\sigma_\eta^2}}\right)\right]$$
$$\times \exp\left(-\sum_{l=0}^{K_\epsilon-1} |g_l|^2\right) \times \sum_{k=0}^{K-1} \frac{r}{b_k} \exp\left(-\frac{r^2+a_k}{2b_k}\right) I_0\left(\frac{\sqrt{a_k}}{b_k}r\right) \prod_{\substack{\tilde{k}=0 \\ \tilde{k}\neq k}}^{K-1} \left[1 - Q_1\left(\sqrt{\frac{a_{\tilde{k}}}{b_{\tilde{k}}}}, \frac{r}{\sqrt{b_{\tilde{k}}}}\right)\right] dg_0 \cdots dg_{K_\epsilon-1} dr \tag{22}$$

$$I_{\boldsymbol{\chi}}(h_{\mathrm{FAS}}) = \log_2 |\boldsymbol{\chi}| + \frac{1}{|\boldsymbol{\chi}|} \iint_{\mathbb{C}} \sum_{i=1}^{\log_2|\boldsymbol{\chi}|} \sum_{b=0}^{1} \sum_{x\in\boldsymbol{\chi}_i^{(b)}} p(\tilde{x}|x,h_{\mathrm{FAS}}) \log_2 \frac{\sum_{x\in\boldsymbol{\chi}_i^{(b)}} p(\tilde{x}|x,h_{\mathrm{FAS}})}{\sum_{x\in\boldsymbol{\chi}} p(\tilde{x}|x,h_{\mathrm{FAS}})} d\tilde{x} \tag{24}$$

$$I_{\mathrm{FAS}} = \int_{r=0}^\infty I_{\boldsymbol{\chi}}(r) p(r) dr$$
$$\approx \log_2 |\boldsymbol{\chi}| + \frac{1}{|\boldsymbol{\chi}| \pi^{K_\epsilon}} \int_0^\infty \iint_{\mathbb{C}} \cdots \iint_{\mathbb{C}} \sum_{i=1}^{\log_2|\boldsymbol{\chi}|} \sum_{b=0}^{1} \sum_{x\in\boldsymbol{\chi}_i^{(b)}} p(\tilde{x}|x,r) \log_2 \frac{\sum_{x\in\boldsymbol{\chi}_i^{(b)}} p(\tilde{x}|x,r)}{\sum_{x\in\boldsymbol{\chi}} p(\tilde{x}|x,r)} \times \exp\left(-\sum_{l=0}^{K_\epsilon-1} |g_l|^2\right)$$
$$\times \sum_{k=0}^{K-1} \frac{r}{b_k} \exp\left(-\frac{r^2+a_k}{2b_k}\right) I_0\left(\frac{\sqrt{a_k}}{b_k}r\right) \prod_{\substack{\tilde{k}=0 \\ \tilde{k}\neq k}}^{K-1} \left[1 - Q_1\left(\sqrt{\frac{a_{\tilde{k}}}{b_{\tilde{k}}}}, \frac{r}{\sqrt{b_{\tilde{k}}}}\right)\right] d\tilde{x} dg_0 \cdots dg_{K_\epsilon-1} dr \tag{25}$$

$$I(\boldsymbol{H}) = \log_2 |\boldsymbol{\chi}| + \frac{1}{NF} \sum_{n=0}^{N-1} \sum_{f=0}^{F-1} \sum_{i=1}^{\log_2|\boldsymbol{\chi}|} \sum_{b=0}^{1} \frac{\sum_{x\in\boldsymbol{\chi}_i^{(b)}} p(\tilde{x}[f,n]|x,h_{k^*}[f,n])}{\sum_{x\in\boldsymbol{\chi}} p(\tilde{x}[f,n]|x,h_{k^*}[f,n])} \log_2 \frac{\sum_{x\in\boldsymbol{\chi}_i^{(b)}} p(\tilde{x}[f,n]|x,h_{k^*}[f,n])}{\sum_{x\in\boldsymbol{\chi}} p(\tilde{x}[f,n]|x,h_{k^*}[f,n])} \tag{32}$$

In FAS-OFDM, the effective SNR, Γ_{eff}, can be derived from the inverse function of the BICM capacity $I(\cdot)$ as

$$\Gamma_{\mathrm{eff}} = \alpha I^{-1}\left[I(\boldsymbol{H})\right], \tag{34}$$

where $I(\boldsymbol{H})$ is the average BICM capacity of the $F \times N$ grid calculated as per (32), and α is the adjustment factor, which can be tailored to correspond to the modulation constellation and code rate of the chosen CQI. The MMSE method is used to calibrate the adjustment factor α, given by

$$\alpha_{\mathrm{opt}} = \arg\min_\alpha \left\{\sum_{i=1}^{N_c} |\Delta e_i(\alpha)|^2\right\}, \tag{35}$$

where

$$\Delta e_i(\alpha) = \log_{10} \Gamma_{\mathrm{eff}}^{(i)}(\alpha) - \log_{10} \Gamma_{\mathrm{LUT}}^{(i)}, \tag{36}$$

where N_c denotes the number of channel realizations, $\Gamma_{\mathrm{eff}}^{(i)}(\alpha)$ and $\Gamma_{\mathrm{LUT}}^{(i)}$ are the effective SNR calculated by (34) and the SNR from the LUT, respectively.

The latency of CQI-based AMC mechanism stems from CQI generation, uplink CQI feedback, transmitter processing delays, and downlink scheduling delays. The latter three factors remain consistent with conventional systems, since we

calculate and map the effective SNR to the pre-defined LUT. However, the additional delay is caused by the complexity of calculating the effective SNR as in (34) to generate CQI. Still, the increase in complexity is marginal since the $\boldsymbol{H}$ in (34) is confined to the channel of the optimal port.

IV. APPLICATION TO 5G NR SYSTEM AND SIMULATION RESULTS

In this section, we employ the port selection metric and the AMC mechanism discussed in Section III to 5G NR systems. The transmission of physical data share channel (PDSCH) is considered. In the procedures associated with PDSCH [58], the channel coding includes the code block segmentation, the cyclic redundancy check (CRC) attachment, the low-density parity-check (LDPC) encoding, and the rate matching [59]. The length of uncoded bits in a subframe, N_a, corresponds to the transmit block size (TBS), while the length of transmission data bits is determined by $N_b = N_{\mathrm{RE}} \times Q_m$, with $N_{\mathrm{RE}} = N_s = N'_{\mathrm{RE}} \times N_{\mathrm{PRB}}$ being the number of resource elements allocated for data transmission in a subframe, and N'_{RE} is the number of resource elements per physical resource block (PRB). The

This article has been accepted for publication in IEEE Transactions on Communications. This is the author's version which has not been fully edited and content may change prior to final publication. Citation information: DOI 10.1109/TCOMM.2025.3591751

7

overall code rate can be expressed as

$$\text{CR} = N_a/N_b = \text{TBS}/(N_{\text{RE}} \times Q_m). \tag{37}$$

The BICM efficiency is thereby denoted as

$$E_{\text{BICM}} = \text{CR} \times Q_m = \text{TBS}/N_{\text{RE}} \text{ [bit/channel use]}. \tag{38}$$

Following constellation mapping, the resultant symbol sequence is mapped to the PRBs for OFDM transmission [60]. In this paper, we focus on the FAS performance, operating under the assumptions of static resource allocation and constant power allocation. Thus, the transmission symbol grid $\boldsymbol{X}$ comprises $N = N_{\text{symb}}^{\text{subframe}}$ OFDM symbols and $F = N_{\text{PRB}} \times N_{\text{sc}}^{\text{RB}}$ subcarriers, where $N_{\text{symb}}^{\text{subframe}}$ is the number of OFDM symbols per subframe, N_{PRB} refers to the number of PRBs, and $N_{\text{sc}}^{\text{RB}}$ denotes the number of subcarriers per resource block (RB). The symbol matrix $\boldsymbol{X}$ is OFDM modulated to produce a time-domain symbol sequence for transmission.

The overall system throughput can be calculated as

$$\gamma = \text{TBS}/T_{\text{subframe}} \text{ [bps]}, \tag{39}$$

where $T_{\text{subframe}} = 1 \text{ ms}$ is the duration of a subframe. The overall spectrum efficiency is then calculated as

$$E = \gamma/\text{BW} \text{ [bps/Hz]}, \tag{40}$$

where BW denotes the bandwidth. The relationship between the spectrum efficiency in (40) and the BICM efficiency in (38) can be expressed as

$$E = E_{\text{BICM}}(1 - \epsilon_{\text{RS}})(1 - \epsilon_{\text{CP}})(1 - \epsilon_{\text{GB}}), \tag{41}$$

in which $\epsilon_{\text{RS}}, \epsilon_{\text{CP}}, \epsilon_{\text{GB}}$ account for the overhead of reference signals, CP, guard bands (GB), respectively, and are given by

$$\begin{cases} \epsilon_{\text{RS}} = 1 - \dfrac{N_{\text{RE}}}{N_{\text{PRB}} \times N_{\text{sc}}^{\text{RB}} \times N_{\text{symb}}^{\text{subframe}}}, \\ \epsilon_{\text{CP}} = \dfrac{T_{\text{CP}}}{T_{\text{subframe}}}, \\ \epsilon_{\text{GB}} = 1 - \dfrac{\text{ABW}}{\text{BW}}. \end{cases} \tag{42}$$

In (42), T_{CP} is the duration of CP, and $\text{ABW} = N_{\text{PRB}} \times N_{\text{sc}}^{\text{RB}} \times \Delta f$ denotes the available bandwidth.

The signals are transmitted over the 3GPP TDL channel [61] based on the correlation matrix $\boldsymbol{\Sigma}$ in (5). The power and delay profile for the TDL channel are detailed in [61, Clause 7.7.2]. For AMC, CQI is represented by 4 bits, ranging from 0 to 15. CQI is fed back as a part of the CSI report to the base station via the physical uplink control channel (PUCCH). As discussed in Section III-D, uplink CQI feedback and the subsequent procedures are backward compatible with the conventional 5G NR system. Every CQI, aside from CQI 0, corresponds to a combination of code rate and modulation constellation. We use [58, Table 5.2.2.1-2], and the combinations of code rate and modulation are outlined in Table II. The user equipment (UE) assesses and reports back the CQI to next generation NodeB (gNB), which subsequently selects a modulation and coding scheme (MCS) from the 32 MCSs defined in [58, Table 5.1.3.1-1] for the UE that aligns with the constellation and closely matches the code rate by the CQI.

TABLE I
SIMULATION PARAMETERS

Parameter	Value			
Normalized size of FAS W_1 or W_2	0.2, 0.5, 1, 2, 5			
Number of ports K_1 or K_2	From 1 to 20			
Subcarrier spacing Δf	15 kHz			
Number of subcarriers per RB $N_{\text{sc}}^{\text{RB}}$	12			
Number of symbols per subframe $N_{\text{symb}}^{\text{subframe}}$	14			
Number of resource elements in a PRB N_{RE}'	156			
Cyclic prefix (CP)	Normal			
Bandwidth (BW) [MHz]	1.4	5	10	20
Number of PRBs N_{PRB}	6	25	50	100
FFT Size N_{fft}	128	512	1024	2048
Channel Model	TDL-C channel			
Channel Estimation	Perfect			
Delay spread	10, 30, 100, 300, 1000 ns			
Maximum Doppler frequency	0, 30, 100, 300, 1000 Hz			
Demapping Scheme	Max-Log-MAP			
Decoding Scheme	Min-Sum with 50 iterations			

In the simulations, the system parameters are summarized in Table I. Normal CP is used in the simulations, resulting in a CP duration of $T_{\text{CP}} = 66.67 \ \mu\text{s}$ out of $T_{\text{subframe}} = 1 \text{ ms}$. Section IV-A presents only the results in narrowband system, while others focus on the wideband link-level simulations. We mainly focus on the wideband system with a bandwidth of 5 MHz, though comparisons with systems utilizing different bandwidths are addressed in Section IV-B. In Sections IV-B and IV-C, we employ static MCS 7 with target code rate of $526/1024$ and QPSK modulation from [58, Table 5.1.3.1-1], while Sections IV-D, IV-E, and IV-F evaluate the AMC using the CQI table in [58, Table 5.2.2.1-2]. Sections IV-B, IV-D, IV-E, and IV-F specifically focus on the scenarios with a short delay spread of 30 ns and a maximum Doppler frequency of 30 Hz, while Section IV-C assesses the system under varying delay spreads and maximum Doppler frequency profiles.

A. Results in Narrowband Channels

In this subsection, we present simulation results to study the accuracy of the approximated ASEP and BICM capacity discussed in Section III-B. Although the channel model h_k in (4) has been significantly simplified by $\tilde{h}_k$, the ASEP and BICM capacity in (22) and (25) remain challenging to compute as they involve a K_ϵ-fold complex integral. Therefore, we obtain the approximated results in this subsection based on the channel model $\tilde{h}_k$ in (19) through Monte Carlo integration.

Fig. 2 presents the simulation symbol error rate (SER) using the exact channel model h_k, and the Monte Carlo integration results of ASEP using the exact channel model h_k and the approximated channel model $\tilde{h}_k$. The result of the FPA system with a configuration of $K = 1 \times 1$ is also presented for comparison. As expected, FAS outperforms FPA. Compared to the simulation SER, ASEP calculated by h_k is accurate and that obtained by $\tilde{h}_k$ serves as the lower bound. As K_ϵ increases, the bounds approach quickly to the curve obtained by h_k. The approximation is considered sufficiently accurate when $K_\epsilon = 10$ for this FAS configuration.
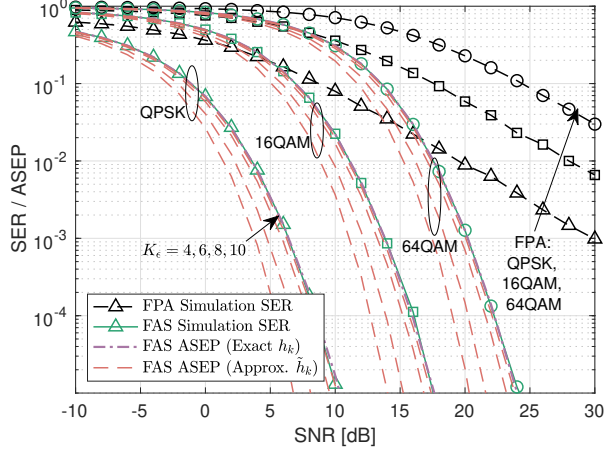
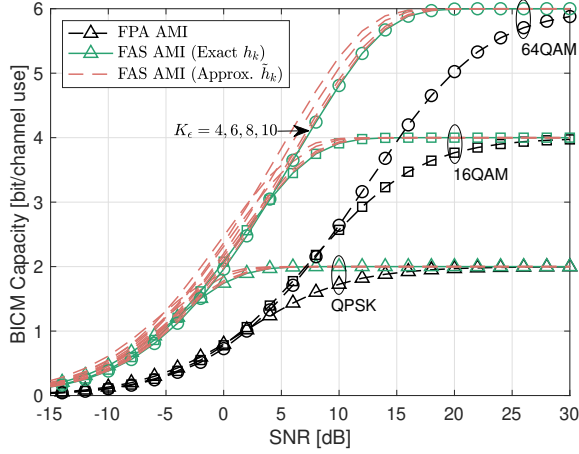Fig. 2. SER and ASEP versus SNR with $W = 1\lambda \times 1\lambda$ and $K = 20 \times 20$.

Fig. 3. BICM capacity versus SNR with $W = 1\lambda \times 1\lambda$ and $K = 20 \times 20$.

Fig. 3 illustrates the BICM capacity using the exact channel model h_k and the approximated channel model $\tilde{h}_k$. We observe that FAS achieves higher BICM capacity than FPA. When SNR is large, BICM capacity is constrained by Q_m, representing the maximum transmission capability of the modulation constellation χ. Compared to the curve obtained from h_k, the approximated BICM capacity resulting from $\tilde{h}_k$ serves as the upper bound. The bounds approach to the exact curve as K_ϵ increases.
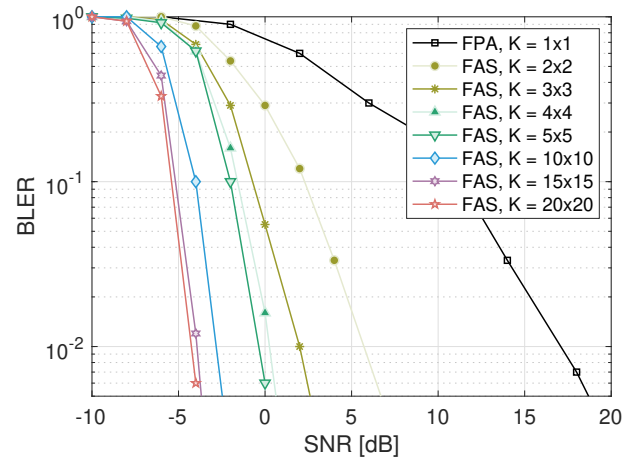
B. BLER Performance

Fig. 4 demonstrates the BLER performance of the wideband FAS-OFDM system, for a comparative analyses against various configurations of FAS. The BLER of the FPA-based system with a configuration of $K = 1 \times 1$ distributed across a 2D area of $W = W_1\lambda \times W_2\lambda$ is also included for comparison. As can be seen, FAS outperforms FPA greatly, even when the FAS has a relatively small size of $W = 0.2\lambda \times 0.2\lambda$, or very few ports, specifically $K = 2 \times 2$. When the physical size of FAS, W, is small, the performance enhancement through an increase in the number of antenna ports is considerably
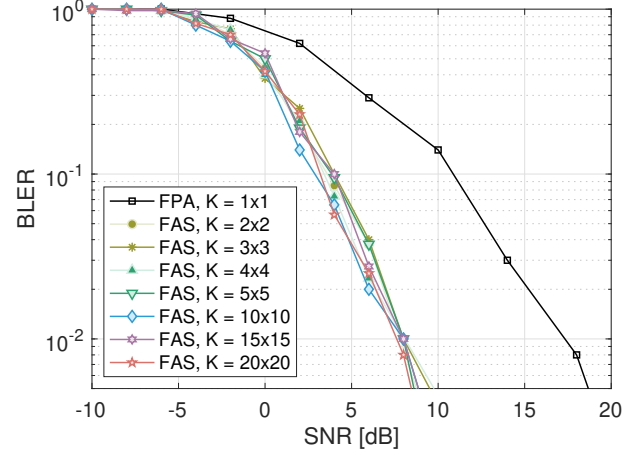
(a) $W = 0.2\lambda \times 0.2\lambda$
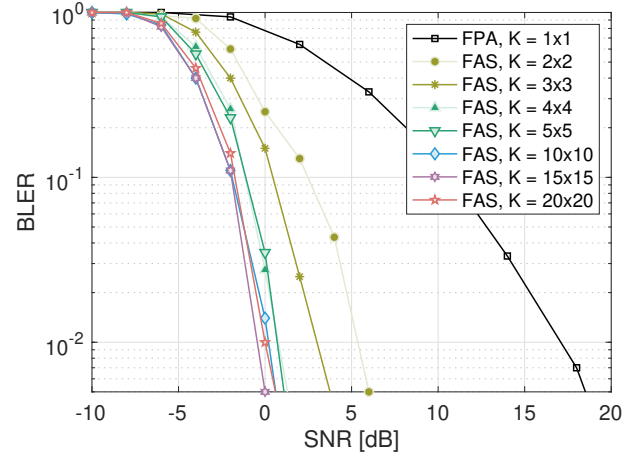
(b) $W = 1\lambda \times 1\lambda$

(c) $W = 5\lambda \times 5\lambda$

Fig. 4. BLER performance comparison for different number of FAS antenna ports, K. Results are presented for MCS 7, with FAS physical size of (a) $W = 0.2\lambda \times 0.2\lambda$, (b) $W = 1\lambda \times 1\lambda$, and (c) $W = 5\lambda \times 5\lambda$.

constrained due to significant correlation among the antenna ports. For instance, when $W = 0.2\lambda \times 0.2\lambda$, as illustrated in Fig. 4(a), a performance gain of 10 dB is achieved if $\text{BLER} = 10^{-2}$ is to be satisfied, corresponding to an increase in the number of ports from $K = 2 \times 2$ to 20×20. However, with an appropriately scaled physical size, BLER performance exhibits improvement as the number of antenna ports escalates until a saturation point is reached, beyond which no further enhancement in performance is observable with additional antenna ports. For example, when the physical size is established as $W = 5\lambda \times 5\lambda$ in Fig. 4(c), a performance gain of 11 dB is observed when $K = 2 \times 2$, increasing to 21 dB for $K = 20 \times 20$. The number of ports to reach saturation is higher for larger size W. In Fig. 4(a), the point of saturation is identified at $K = 2 \times 2$ for $W = 0.2\lambda \times 0.2\lambda$, while it extends to approximately $K = 10 \times 10$ for $W = 1\lambda \times 1\lambda$ in Fig. 4(b), and approaches $K = 20 \times 20$ for $W = 5\lambda \times 5\lambda$ in Fig. 4(c). Moreover, comparing the FPA results with different physical size, the performance of FPA remains invariant with respect to alterations in the physical size of the antenna.

Comparing Fig. 4 vertically, it reveals that the performance gain of FAS is markedly higher with larger physical size, particularly when the number of antenna ports K is deemed sufficient. With a limited number of FAS ports, such as $K = 2 \times 2$, the BLER performance exhibits an upward trend correlating with the physical size until reaching the saturation point rapidly. Specifically, the performance of $W = 5\lambda \times 5\lambda$ is similar to that of $W = 5\lambda \times 5\lambda$ when $K = 2 \times 2$. At the saturation point, the correlation among the antenna ports becomes negligible, and the performance is predominantly constrained by the limited number of the antenna ports. Conversely, with an adequate number of antenna ports, such as $K = 20 \times 20$, FAS demonstrates superior performance gains as the physical size increases. For instance, the SNR required to achieve $\text{BLER} = 10^{-2}$ is approximately 7 dB with $W = 0.2\lambda \times 0.2\lambda$, when $K = 20 \times 20$. This SNR decreases to 0 dB when the size increases to $W = 1\lambda \times 1\lambda$, and further decreases to -4 dB with $W = 5\lambda \times 5\lambda$.

The results in Fig. 5 study the BLER in relation to bandwidth. The results indicate a modest performance degradation with increasing bandwidth. We see that FAS-OFDM performs better at narrower bandwidths. This phenomenon is attributed to the reality that systems operating with broader bandwidths incorporate more subcarriers, rendering them more susceptible to frequency-selective fading. In a high-dynamic channel, the subframe average SNR in (12) tends to converge toward the average SNR Θ, which may hinder resolution among the fluid antenna ports. Nevertheless, the simulation results indicate that the observed performance degradation remains minor. FAS-OFDM continues to provide considerable performance gains even at a bandwidth of 20 MHz. Notably, the performance at the bandwidth of 1.4 MHz is slightly worse than that at 5 MHz bandwidth. This discrepancy ascribed to the actual spectral efficiency of MCS 7 in the 1.4 MHz bandwidth system being slightly higher than that in the 5 MHz bandwidth system, in accordance with the TBS determination of 5G NR.

(a) $W = 1\lambda \times 1\lambda$

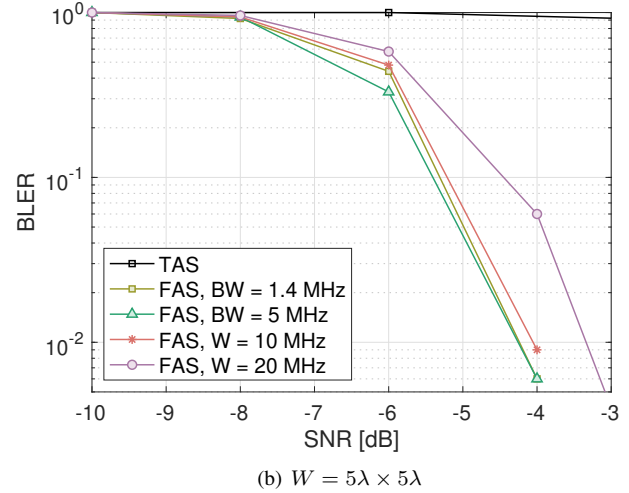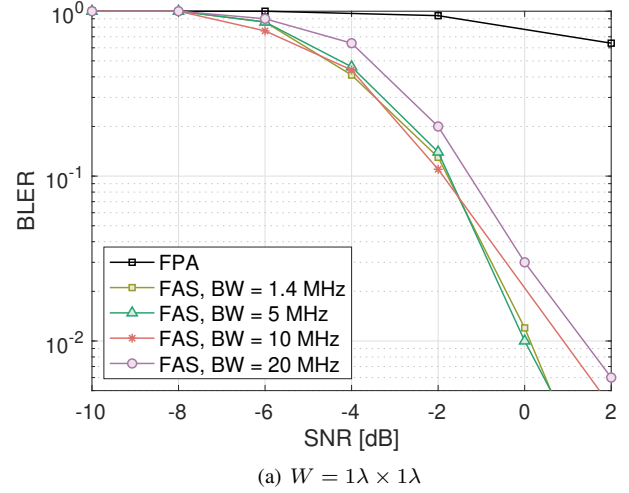
(b) $W = 5\lambda \times 5\lambda$

Fig. 5. BLER performance comparison for different bandwidths. Results are presented for MCS7, with $K = 20 \times 20$ antenna ports over the FAS with physical size of (a) $W = 1\lambda \times 1\lambda$ and (b) $W = 5\lambda \times 5\lambda$.

C. Mobility Evaluation

To evaluate the performance of FAS-OFDM under mobility scenarios, simulations are conducted under time-varying delay spread and maximum Doppler shift profiles. Fig. 6 presents the results associated with different delay spread profiles. Delay spread is closely related to the propagating environment. The adopted delay spread profiles, ranging from 10 ns to 1000 ns, are categorized according to [61, Table 7.7.3-1] as very short, short, nominal, long, and very long delay spreads, respectively. As can be seen, the BLER performance degrades as the delay spread increases, particularly in the system exhibiting long or very long delay spreads. Performance degradation occurs as the coherence bandwidth is smaller than the system bandwidth. Specifically, for a long delay spread (DS = 300 ns), the coherence bandwidth is $\text{BW}_c = 3.3$ MHz, while the coherence bandwidth for a very long delay spread (DS = 1000 ns) is $\text{BW}_c = 1$ MHz, both of which fall below the system bandwidth of BW = 5 MHz. Consequently, frequency-selective fading becomes more severe, leading to increased ISI that distorts

This article has been accepted for publication in IEEE Transactions on Communications. This is the author's version which has not been fully edited and content may change prior to final publication. Citation information: DOI 10.1109/TCOMM.2025.3591751

10

(a) $W = 1\lambda \times 1\lambda$

(a) $W = 1\lambda \times 1\lambda$

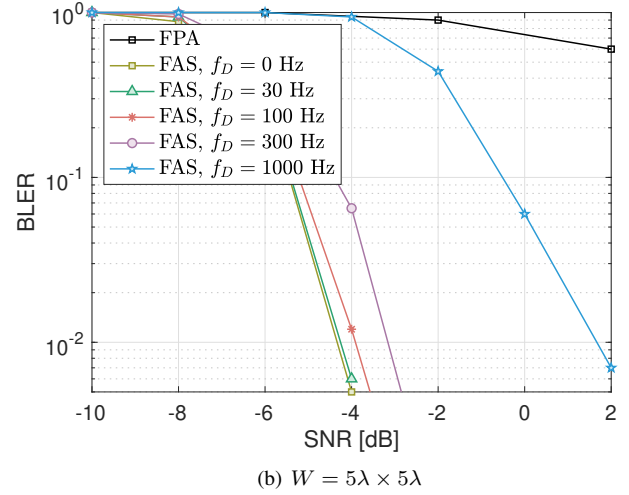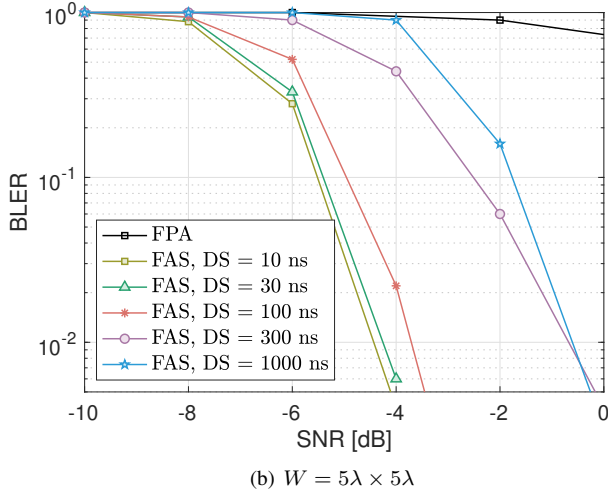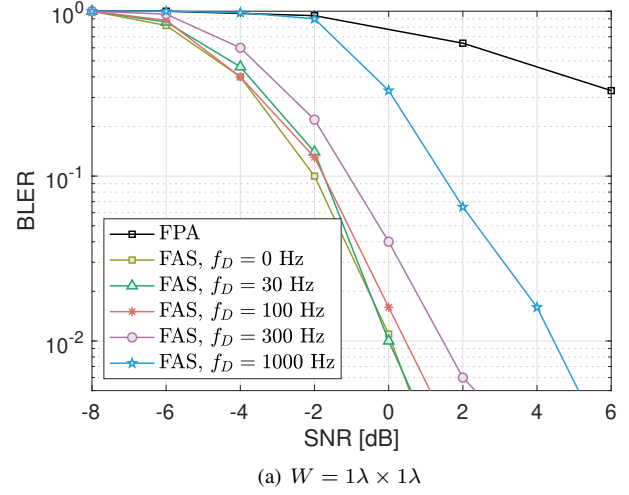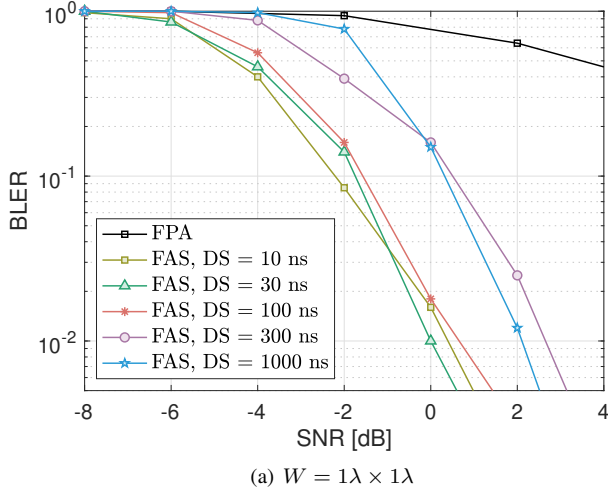(b) $W = 5\lambda \times 5\lambda$

(b) $W = 5\lambda \times 5\lambda$

Fig. 6. BLER performance comparison for different delay spread. Results are presented for MCS7, with $K = 20 \times 20$ antenna ports over the FAS with physical size of (a) $W = 1\lambda \times 1\lambda$ and (b) $W = 5\lambda \times 5\lambda$.

Fig. 7. BLER performance comparison for different delay spread. Results are presented for MCS7, with $K = 20 \times 20$ antenna ports over the FAS with physical size of (a) $W = 1\lambda \times 1\lambda$ and (b) $W = 5\lambda \times 5\lambda$.

the signal. But the performance degradation remains relatively small, amounting to less than 2 dB or 4 dB for configurations of $W = 1\lambda \times 1\lambda$ or $5\lambda \times 5\lambda$, respectively. It can still achieve considerable performance gain compared to FPA.

In Fig. 7, we provide the BLER results for various Doppler shift (f_D) values. Considering carrier frequency of 5 GHz, a Doppler frequency of $f_D = 1000$ Hz corresponds to the relative velocity of 216 km/h of the UE, which represents a very high-speed scenario. The maximum Doppler frequencies of $f_D = 300$ and 100 Hz correspond to typical vehicular scenarios with relative velocities of 64.8 and 21.6 km/h, while $f_D = 30$ Hz indicates a pedestrian scenario with a velocity of 6.48 km/h, and $f_D = 0$ Hz reflects a stationary scenario. The BLER performance demonstrates some decline in the mobile scenarios, as expected. The performance degradation observed in the pedestrian scenario is negligible, while in vehicular scenarios, it remains below 2 dB. However, in the high-speed vehicular scenario, the performance degradation is more substantial, approximately 4.5 dB for $W = 1\lambda \times 1\lambda$ and about 6 dB for $W = 5\lambda \times 5\lambda$. Nevertheless, the performance

remains much better than that of the FPA system. This notable performance degradation can be attributed to a low coherence time ($T_c = 1/f_D = 1$ ms), which is equivalent to the duration of a subframe. As such, time-selective fading becomes severe, causing considerable performance degradation.

D. AMC

As introduced in Section III-D, we first conduct simulations of 15 cases in the single-input single-output (SISO) system over AWGN channels, with results presented in Fig. 8. By considering a criterion of BLER $= 0.1$, the SNR threshold for the LUT (look-up table) can be deduced through linear fitting of the simulated results, as detailed in Table II under the designation of Γ_{LUT}. Subsequently, simulations of FAS-OFDM are performed to ascertain the optimal adjustment factor α. In this subsection, we consider the system featuring FAS with $K = 20 \times 20$ ports uniformly distributed over a physical size of $W = 1\lambda \times 1\lambda$. The adjustment factors related to the 15 CQI indices are listed in the final column of Table II.

TABLE II
SNR THRESHOLD AND OPTIMAL ADJUSTMENT FACTOR

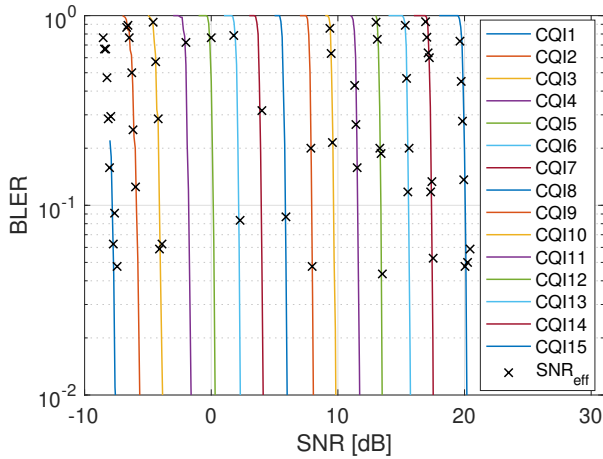| CQI index	Modulation	Code Rate ×1024	SNR threshold Γ_{LUT} (dB)	α
0	Out of range			
1	QPSK	78	−7.84	0.97
2	QPSK	120	−5.94	0.76
3	QPSK	193	−4.11	0.98
4	QPSK	308	−1.80	1.00
5	QPSK	449	0.13	1.00
6	QPSK	602	2.16	0.95
7	16QAM	378	3.93	1.00
8	16QAM	490	5.83	1.00
9	16QAM	616	7.93	0.97
10	64QAM	466	9.67	0.97
11	64QAM	567	11.56	0.96
12	64QAM	666	13.38	0.98
13	64QAM	772	15.57	0.96
14	64QAM	873	17.39	0.96
15	64QAM	948	20.03	0.92

Fig. 8. Effective SNR mapping for AMC in the FAS-OFDM system with $K = 20 \times 20$ FAS antenna ports over the physical size of $W = 1\lambda \times 1\lambda$.

(a) BW = 5 MHz

(b) BW = 20 MHz

Fig. 9. Throughput against SNR in dB of the FAS-OFDM system. Results are presented for (a) 5 MHz bandwidth and (b) 20 MHz bandwidth.

Fig. 8 presents the effective SNR mapping for FAS-OFDM operating under the TDL-C channel, characterized by DS = 30 ns and $f_D = 30$ Hz. The solid lines represent the SNR-BLER curves for the SISO system over the AWGN channel, whereas the black 'X' markers depict the BLER against the effective SNR as mapped by (34), using the adjustment factors α in Table II. The 'X' points in Fig. 8 are relatively concentrated on the AWGN curves, which indicates that the AMC, supported by the effective SNR mapping in (34), is highly accurate and effectively reflects the channel quality of FAS-OFDM.

E. Throughput

Fig. 9 presents the throughput of FAS-OFDM using the 15 CQI indices. The results are based on the TDL channel, with DS = 30 ns and $f_D = 30$ Hz. The results depicted in this figure are based on the criterion of BLER = 0.1. The SNR is the transmission SNR when BLER = 0.1, and the throughput is calculated as $\gamma \times (1 - \text{BLER})$, where γ is the overall system throughput given in (39). Simulations for the FPA system are
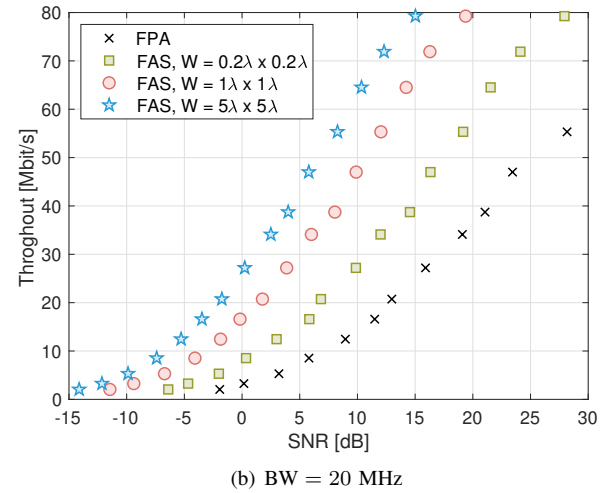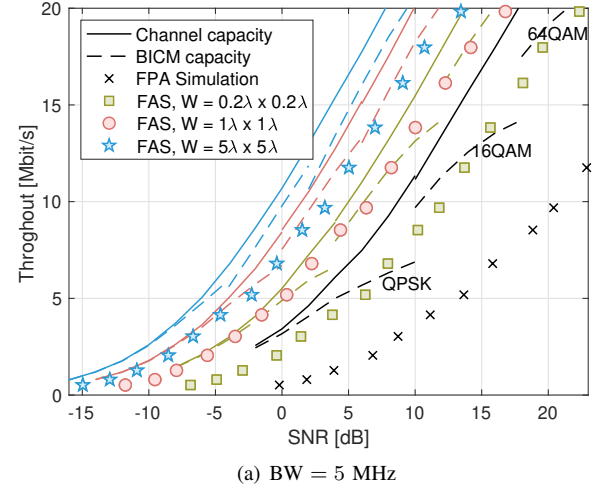
also conducted for comparison. For the FAS-OFDM system, the FAS configuration involves $K = 20 \times 20$ ports uniformly distributed over varying sizes: $W = 0.2\lambda \times 0.2\lambda$, $1\lambda \times 1\lambda$, and $5\lambda \times 5\lambda$. Additionally, the channel capacity and the BICM capacity are also plotted for comparison within the 5 MHz bandwidth system in Fig. 9(a). These two rates are calculated in accordance with Section III-C, with adjustments made to account for the RS, CP, and GB overheads, as specified in (41). The BICM capacity calculations utilize QPSK, 16QAM, and 64QAM in low, medium, and high SNR region, respectively.

As expected, the simulation results are upper-bounded by the semi-analytical capacity results. Note that the gaps between the simulations and the semi-analytical results are minimal in the FAS-OFDM system, especially when the size of FAS is large. This observation may indicate that FAS effectively approaches the capacity. Moreover, the throughput in the FAS-OFDM system shows a considerable improvement over that of the FPA system, with more throughput gain as the size of FAS increases. A commonly used SNR value of interest for reception is 10 dB. Under this particular condition, the FPA system
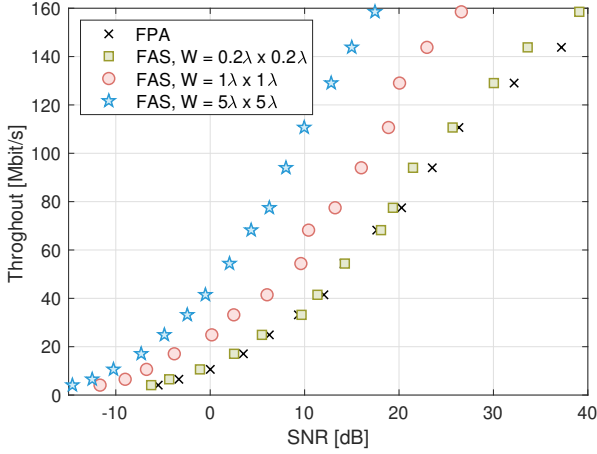
This article has been accepted for publication in IEEE Transactions on Communications. This is the author's version which has not been fully edited and content may change prior to final publication. Citation information: DOI 10.1109/TCOMM.2025.3591751

12

Fig. 10. Throughput against SNR in dB of the 2×2 MIMO-FAS-OFDM system for a bandwidth of 20 MHz.

provides throughput of 3.62 Mbit/s and 14.15 Mbit/s for the 5 MHz and 20 MHz bandwidth, respectively, corresponding to a spectral efficiency of 0.7 bit/s/Hz. Conversely, the FAS-OFDM system achieves throughput of 8.39 Mbit/s and 27.63 Mbit/s, even with a relatively small FAS size $W = 0.2\lambda \times 0.2\lambda$, effectively doubling the throughput of the FPA system. With a configuration of $W = 1\lambda \times 1\lambda$, the throughput increases to 13.81 Mbit/s for 5 MHz bandwidth and 47.43 Mbit/s for 20 MHz bandwidth. This performance further escalates, reaching 17.18 Mbit/s and 62.97 Mbit/s with the $W = 5\lambda \times 5\lambda$ FAS configuration. Overall, the FAS-OFDM system significantly enhances throughput, achieving improvements ranging from 95% to 375% compared to the FPA system.

F. MIMO-FAS-OFDM

The FAS-OFDM system can be extended to a MIMO communication system. In this subsection, we consider a simple 2×2 MIMO-FAS-OFDM system, where the transmitter employs two conventional FPAs to transmit two separate data streams, and a FAS with two activated ports is equipped at the receiver. The FAS ports with the first two highest metrics (10) are activated for receiving, and MMSE is utilized for multi-stream detection. Fig. 10 presents the throughput of this 2×2 MIMO-FAS-OFDM system with a bandwidth of 20 MHz. For the benchmark FPA-based MIMO system, the receiver antenna configuration can be viewed as a one-dimensional FAS (1D-FAS) with configuration of $K = 2$ ports distributed along the linear space of $W = \sqrt{W_1^2 + W_2^2}\lambda$.

As can be seen, the throughput doubles with a modest increase in SNR, compared to the throughput of the SISO system as illustrated in Fig. 9(b). The throughput of the MIMO-FAS-OFDM system exhibits an improvement over that of the FPA-based system. This performance gain increases with the size of FAS. At an SNR of 10 dB, the FPA-based 2×2 MIMO system achieves a throughput of 33.2 Mbit/s. In contrast, the throughput rises to 59.3 Mbit/s in the 2×2 MIMO-FAS-OFDM system with a FAS configuration of $W = 1\lambda \times 1\lambda$,

TABLE III
COMPARISONS BETWEEN FAS AND FPA

Scheme	Channel Estimation	Spectral Efficiency	BLER Perf.
FAS	High	High	Low SNR
FPA	Moderate	Low	High SNR

and further escalates to 110.7 Mbit/s with the configuration of $W = 5\lambda \times 5\lambda$.

Notably, the FAS with size of $W = 0.2\lambda \times 0.2\lambda$ yields only marginal gains over the FPA-based system. This limited improvement can be attributed to the compact size of FAS, which results in relatively high mutual coupling between the two activated ports. Implementing an appropriate MIMO beamforming design or employing FAS at the transmitter side can enhance the overall performance of the MIMO-FAS-OFDM system. Nevertheless, deploying FAS at the transmitter will be trickier, and several challenges related to CSI feedback for MIMO beamforming or FAS port selection need to be addressed. Future work may focus on overcoming these challenges to fully realize the potential of the FAS.

G. Summary of Performance Evaluation

Section IV-A evaluates SER in the uncoded FAS system, while Sections IV-B and IV-C evaluate the BLER performance of FAS-OFDM. Results demonstrate that FAS outperforms state-of-the-art FPA. FAS can achieve the same error rate performance with lower SNR. With AMC established and validated in Section IV-D, Section IV-E compared the throughput of FAS with that of FPA, and Section IV-F extended the throughput comparison to a simple 2×2 MIMO context. It reveals that FAS achieves higher throughput than FPA, indicating that FAS can achieve higher spectral efficiency compared to the FPA scenario. However, the FAS-OFDM system requires more overhead for channel estimation. Table III summarizes the performance comparisons between FAS and the state-of-the-art FPA-based system. In summary, FAS-OFDM can achieve better BLER performance and higher spectral efficiency with a higher requirement of channel estimation.

V. CONCLUSION

In this paper, we integrated FAS within the OFDM framework to address the challenges of utilizing FAS for wideband communications. We proposed a comprehensive framework for FAS-OFDM that includes channel-aware port selection metrics and the AMC mechanism. The proposed system utilizes the PDSCH procedures in the 5G NR specifications. The link-level simulation results showed great improvements in the BLER and throughput, even in a small space, highlighting the great potential of FAS for future wireless communications.

REFERENCES

[1] Ericsson, "Co-creating a cyber-physical world," Available [Online]: https://www.ericsson.com/en/reports-and-papers/white-papers/co-creating-a-cyber-physical-world, Last Accessed on 2024-08-12.

[2] J. G. Andrews, T. E. Humphreys and T. Ji, "6G Takes Shape," *IEEE BITS Inf. Theory Mag.*, early access, doi:10.1109/MBITS.2024.3504521, Nov. 2024.

This article has been accepted for publication in IEEE Transactions on Communications. This is the author's version which has not been fully edited and content may change prior to final publication. Citation information: DOI 10.1109/TCOMM.2025.3591751

13

[3] Z. Zhang *et al.*, "6G wireless networks: Vision, requirements, architecture, and key technologies," *IEEE Veh. Technol. Mag.*, vol. 14, no. 3, pp. 28–41, Sept. 2019.

[4] W. Saad, M. Bennis, and M. Chen, "A vision of 6G wireless systems: Applications, trends, technologies, and open research problems," *IEEE Netw.*, vol. 34, no. 3, pp. 134–142, May/Jun. 2020.

[5] F. Tariq *et al.*, "A speculative study on 6G," *IEEE Wireless Commun.*, vol. 27, no. 4, pp. 118–125, Aug. 2020.

[6] C.-X. Wang *et al.*, "On the road to 6G: Visions, requirements, key technologies, and testbeds," *IEEE Commun. Surv. & Tut.*, vol. 25, no. 2, pp. 905–974, Secondquarter 2023.

[7] K. K. Wong, K. F. Tong, Y. Zhang, and Z. Zheng, "Fluid antenna system for 6G: When Bruce Lee inspires wireless communications," *Elect. Lett.*, vol. 56, no. 24, pp. 1288–1290, Nov. 2020.

[8] K.-K. Wong, K.-F. Tong, Y. Shen, Y. Chen, and Y. Zhang, "Bruce Lee-inspired fluid antenna system: Six research topics and the potentials for 6G," *Front. Commun. Netw. Sec. Wireless Commun.*, vol. 3, Mar. 2022.

[9] C. Wang *et al.*, "AI-empowered fluid antenna systems: Opportunities, challenges, and future directions," *IEEE Wireless Commun.*, vol. 31, no. 5, pp. 34–41, Oct. 2024.

[10] T. Wu *et al.*, "Fluid antenna systems enabling 6G: Principles, applications, and research directions," *arXiv preprint*, arXiv:2412.03839, 2024.

[11] W. K. New *et al.*, "A tutorial on fluid antenna system for 6G networks: Encompassing communication theory, optimization methods and hardware designs," *IEEE Commun. Surv. & Tutor.*, early access, doi:10.1109/COMST.2024.3498855, 2024.

[12] W.-J. Lu *et al.*, "Fluid antennas: Reshaping intrinsic properties for flexible radiation characteristics in intelligent wireless networks," *IEEE Commun. Mag.*, vol. 63, no. 5, pp. 40–45, May 2025.

[13] L. Zhu and K. K. Wong, "Historical review of fluid antenna and movable antenna," *arXiv preprint*, arXiv:2401.02362v2, 2024.

[14] J. Zheng *et al.*, "Flexible-position MIMO for wireless communications: Fundamentals, challenges, and future directions," *IEEE Wireless Commun.*, vol. 31, no. 5, pp. 18–26, Oct. 2024.

[15] Z. Yang *et al.*, "Pinching antennas: Principles, applications and challenges," *arXiv preprint*, arXiv:2501.10753, 2025.

[16] K. K. Wong, A. Shojaeifard, K.-F. Tong, and Y. Zhang, "Performance limits of fluid antenna systems," *IEEE Commun. Lett.*, vol. 24, no. 11, pp. 2469–2472, Nov. 2020.

[17] K. K. Wong, A. Shojaeifard, K. F. Tong, and Y. Zhang, "Fluid antenna systems," *IEEE Trans. Wireless Commun.*, vol. 20, no. 3, pp. 1950–1962, Mar. 2021.

[18] Y. Huang, L. Xing, C. Song, S. Wang and F. Elhouni, "Liquid antennas: Past, present and future," *IEEE Open J. Antennas & Propag.*, vol. 2, pp. 473–487, Mar. 2021.

[19] Y. Shen *et al.*, "Design and implementation of mmWave surface wave enabled fluid antennas and experimental results for fluid antenna multiple access," *arXiv preprint*, arXiv:2405.09663, May 2024.

[20] R. Wang *et al.*, "Electromagnetically reconfigurable fluid antenna system for wireless communications: Design, modeling, algorithm, fabrication, and experiment," *arXiv preprint*, arXiv:2502.19643v2, 2025.

[21] S. Basbug, "Design and synthesis of antenna array with movable elements along semicircular paths," *IEEE Antennas Wireless Propag. Lett.*, vol. 16, pp. 3059–3062, Oct. 2017.

[22] M. C. Johnson, S. L. Brunton, N. B. Kundtz, and J. N. Kutz, "Sidelobe canceling for reconfigurable holographic metamaterial antenna," *IEEE Trans. Antennas & Propag.*, vol. 63, no. 4, pp. 1881–1886, Apr. 2015.

[23] T. V. Hoang, V. Fusco, T. Fromenteze and O. Yurduseven, "Computational polarimetric imaging using two-dimensional dynamic metasurface apertures," *IEEE Open J. Antennas & Propag.*, vol. 2, pp. 488–497, Mar. 2021.

[24] B. Liu, K. F. Tong, K. K. Wong, C.-B. Chae, and H. Wong, "Be water, my antennas: Riding on radio wave fluctuation in nature for spatial multiplexing using programmable meta-fluid antenna," *arXiv preprint*, arXiv:2502.04693, 2025.

[25] J. Zhang *et al.*, "A novel pixel-based reconfigurable antenna applied in fluid antenna systems with high switching speed," *IEEE Open J. Antennas & Propag.*, vol. 6, no. 1, pp. 212–228, Feb. 2025.

[26] M. Khammassi, A. Kammoun and M.-S. Alouini, "A new analytical approximation of the fluid antenna system channel," *IEEE Trans. Wireless Commun.*, vol. 22, no. 12, pp. 8843–8858, Dec. 2023.

[27] W. K. New, K. K. Wong, H. Xu, K. F. Tong and C.-B. Chae, "Fluid antenna system: New insights on outage probability and diversity gain," *IEEE Trans. Wireless Commun.*, vol. 23, no. 1, pp. 128–140, Jan. 2024.

[28] P. Ramírez-Espinosa, D. Morales-Jimenez, and K. K. Wong, "A new spatial block-correlation model for fluid antenna systems," *IEEE Trans. Wireless Commun.*, vol. 23, no. 11, pp. 15829–15843, Nov. 2024.

[29] J. D. Vega-Sánchez, L. Urquiza-Aguiar, M. C. P. Paredes, and D. P. M. Osorio, "A simple method for the performance analysis of fluid antenna systems under correlated Nakagami-m fading," *IEEE Wireless Commun. Lett.*, vol. 13, no. 2, pp. 377–381, Feb. 2024.

[30] J. D. Vega-Sánchez, A. E. López-Ramírez, L. Urquiza-Aguiar, and D. P. M. Osorio, "Novel expressions for the outage probability and diversity gains in fluid antenna system," *IEEE Wireless Commun. Lett.*, vol. 13, no. 2, pp. 372–376, Feb. 2024.

[31] P. D. Alvim *et al.*, "On the performance of fluid antennas systems under α-μ fading channels," *IEEE Wireless Commun. Lett.*, vol. 13, no. 1, pp. 108–112, Jan. 2024.

[32] W. K. New, K. K. Wong, H. Xu, K. F. Tong, and C.-B. Chae, "An information-theoretic characterization of MIMO-FAS: Optimization, diversity-multiplexing tradeoff and q-outage capacity," *IEEE Trans. Wireless Commun.*, vol. 23, no. 6, pp. 5541–5556, Jun. 2024.

[33] C. Skouroumounis and I. Krikidis, "Fluid antenna with linear MMSE channel estimation for large-scale cellular networks," *IEEE Trans. Commun.*, vol. 71, no. 2, pp. 1112–1125, Feb. 2023.

[34] H. Xu *et al.*, "Channel estimation for FAS-assisted multiuser mmWave systems," *IEEE Commun. Lett.*, vol. 28, no. 3, pp. 632–636, Mar. 2024.

[35] Z. Zhang, J. Zhu, L. Dai, and R. W. Heath Jr, "Successive Bayesian reconstructor for channel estimation in fluid antenna systems," *IEEE Trans. Wireless Commun.*, vol. 24, no. 3, pp. 1992–2006, Mar. 2025.

[36] B. Xu, Y. Chen, Q. Cui, X. Tao, and K. K. Wong, "Sparse Bayesian learning-based channel estimation for fluid antenna systems," *IEEE Wireless Commun. Lett.*, vol. 14, no. 2, pp. 325–329, Feb. 2025.

[37] W. K. New *et al.*, "Channel estimation and reconstruction in fluid antenna system: Oversampling is essential," *IEEE Trans. Wireless Commun.*, vol. 24, no. 1, pp. 309–322, Jan. 2025.

[38] B. Tang *et al.*, "Fluid antenna enabling secret communications," *IEEE Commun. Lett.*, vol. 27, no. 6, pp. 1491–1495, Jun. 2023.

[39] H. Xu *et al.*, "Coding-enhanced cooperative jamming for secret communication in fluid antenna systems," *IEEE Commun. Lett.*, vol. 28, no. 9, pp. 1991–1995, Sept. 2024.

[40] F. R. Ghadi *et al.*, "Physical layer security over fluid antenna systems: Secrecy performance analysis," *IEEE Trans. Wireless Commun.*, vol. 23, no. 12, pp. 18201–18213, Dec. 2024.

[41] F. Rostami Ghadi *et al.*, "On performance of RIS-aided fluid antenna systems," *IEEE Wireless Commun. Lett.*, vol. 13, no. 8, pp. 2175–2179, Aug. 2024.

[42] J. Zhu *et al.*, "Fluid antenna empowered index modulation for RIS-aided mmWave transmissions," *IEEE Trans. Wireless Commun.*, vol. 24, no. 2, pp. 1635–1647, Feb. 2025.

[43] J. Yao *et al.*, "FAS-RIS communication: Model, analysis, and optimization," *IEEE Trans. Veh. Technol.*, doi:10.1109/TVT.2025.3537294, 2025.

[44] A. Salem, K. K. Wong, G. Alexandropoulos, C.-B. Chae, and R. Murch, "A first look at the performance enhancement potential of fluid reconfigurable intelligent surface," *arXiv preprint*, arXiv:2502.17116v1, 2025.

[45] C. Wang *et al.*, "Fluid antenna system liberating multiuser MIMO for ISAC via deep reinforcement learning," *IEEE Trans. Wireless Commun.*, vol. 23, no. 9, pp. 10879–10894, Sept. 2024.

[46] L. Zhou, J. Yao, M. Jin, T. Wu and K. K. Wong, "Fluid antenna-assisted ISAC systems," *IEEE Wireless Commun. Lett.*, vol. 13, no. 12, pp. 3533–3537, Dec. 2024.

[47] J. Zou *et al.*, "Shifting the ISAC trade-off with fluid antenna systems," *IEEE Wireless Commun. Lett.*, vol. 13, no. 12, pp. 3479–3483, Dec. 2024.

[48] K. K. Wong and K. F. Tong, "Fluid antenna multiple access," *IEEE Trans. Wireless Commun.*, vol. 21, no. 7, pp. 4801–4815, Jul. 2022.

[49] K. K. Wong, D. Morales-Jimenez, K. F. Tong, and C. B. Chae, "Slow fluid antenna multiple access," *IEEE Trans. Commun.*, vol. 71, no. 5, pp. 2831–2846, May 2023.

[50] H. Xu *et al.*, "Revisiting outage probability analysis for two-user fluid antenna multiple access system," *IEEE Trans. Wireless Commun.*, vol. 23, no. 8, pp. 9534–9548, Aug. 2024.

[51] N. Waqar, K. K. Wong, K. F. Tong, A. Sharples, and Y. Zhang, "Deep learning enabled slow fluid antenna multiple access," *IEEE Commun. Lett.*, vol. 27, no. 3, pp. 861–865, Mar. 2023.

[52] H. Hong, K. K. Wong, K. F. Tong, H. Shin, and Y. Zhang, "Coded fluid antenna multiple access over fast fading channels," *IEEE Wireless Commun. Lett.*, vol. 14, no. 4, pp. 1249–1253, Apr. 2025.

[53] H. Hong, K. K. Wong, H. Xu, *et al.*, "Downlink OFDM-FAMA in 5G-NR Systems," accepted in *IEEE Trans. Wireless Commun.*, arxiv:2501.06974, 2025.

This article has been accepted for publication in IEEE Transactions on Communications. This is the author's version which has not been fully edited and content may change prior to final publication. Citation information: DOI 10.1109/TCOMM.2025.3591751

14

[54] K. K. Wong, C. B. Chae, and K. F. Tong, "Compact ultra massive antenna array: A simple open-loop massive connectivity scheme," *IEEE Trans. Wireless Commun.*, vol. 23, no. 6, pp. 6279–6294, Jun. 2024.

[55] K. K. Wong, "Transmitter CSI-free RIS-randomized CUMA for extreme massive connectivity," *IEEE Open J. Commun. Soc.*, vol. 5, pp. 6890–6902, 2024.

[56] Y. Chen and T. Xu, "Fluid antenna index modulation communications," *IEEE Wireless Commun. Lett.*, vol. 13, no. 4, pp. 1203–1207, Apr. 2024.

[57] L. Zhu, W. Ma, Z. Xiao and R. Zhang, "Performance analysis and optimization for movable antenna aided wideband communications," *IEEE Trans. Wireless Commun.*, vol. 23, no. 12, pp. 18653–18668, Dec. 2024.

[58] "NR; Physical layer procedures for data," Available [Online]: https://www.3gpp.org/ftp/Specs/archive/38_series/38.214/38214-i40.zip, Last Accessed on 2024-09-23.

[59] "NR; Multiplexing and channel coding," Available [Online]: https://www.3gpp.org/ftp/Specs/archive/38_series/38.212/38212-i40.zip, Last Accessed on 2024-09-23.

[60] "NR; Physical channels and modulation," Available [Online]: https://www.3gpp.org/ftp/Specs/archive/38_series/38.211/38211-i40.zip, Last Accessed on 2024-09-23.

[61] "Study on channel model for frequencies from 0.5 to 100 GHz," Available [Online]: https://www.3gpp.org/ftp/Specs/archive/38~series/38.901/8901-i00.zip, Last Accessed on 2024-04-03.

[62] V. Khandelwal and Karmeshu, "A new approximation for average symbol error probability over log-normal channels," *IEEE Wireless Commun. Lett.*, vol. 3, no. 1, pp. 58–61, Feb. 2014.

[63] G. Caire, G. Taricco and E. Biglieri, "Bit-interleaved coded modulation," *IEEE Trans. Inf. Theory*, vol. 44, no. 3, pp. 927–946, May 1998.